

Research Article

Experimental Study on Echo Characteristics of Multistatic Large-Scale Underwater Complex Target

Zhu Ling-Guo ^{1,2}, Zhao An-Bang ¹, Liu Wen-zhang², Han Jing ²,
Wang Shu-tao ² and Ma Zhong-cheng ³

¹Harbin Engineering University, Harbin 150001, China

²Dalian Scientific Test and Control Technology Institute, Dalian 116013, China

³Science and Technology on Underwater Test and Control Laboratory, Dalian 116013, China

Correspondence should be addressed to Zhao An-Bang; zhaoanbang@hrbeu.edu.cn

Received 5 December 2017; Revised 28 February 2018; Accepted 21 March 2018; Published 12 June 2018

Academic Editor: Muhammad N. Akram

Copyright © 2018 Zhu Ling-Guo et al. This is an open access article distributed under the Creative Commons Attribution License, which permits unrestricted use, distribution, and reproduction in any medium, provided the original work is properly cited.

Target acoustic scattering is the primary characteristic of target echo stealth performance, and it is an important sign of the viability of large-scale complex targets underwater. In a test band, owing to the superposition of scattered waves and the elastic echo produced by shells, liquid tanks, partition plates, ribs, etc., a target exhibits an extremely complex echo phenomenon. Accurate measurement and evaluation of the acoustic scattering characteristics of underwater complex targets can be achieved via experimental research on the echo characteristics of large-scale scaled models. In this study, the contribution and regularity of the strong reflection source of underwater complex targets in various azimuths, structures, and locations were analyzed quantitatively as a basis for in-depth research and understanding of the echo characteristics of underwater complex targets.

1. Introduction

The study of the complex echo characteristics of underwater targets is primarily based on the theory of elastic spherical shell [1, 2], infinite cylindrical shell [3–5], and finite cylindrical shell [6–8] acoustic scattering. In recent years, significant progress has been made in studies on sound scattering of finite cylindrical shells [9–11] with ring ribs and ring-ribbed plates. However, for large-scale underwater complex targets such as submarines, it is difficult to perform accurate theoretical calculation and numerical simulation because of their complex shape and structure.

Experimental research has been performed on pool and lake echo characteristics [12, 13] using models of different scales to verify theoretical research results, which has promoted the development of theoretical prediction and practice. However, because of model size limitations, it is difficult to study ribbed plates, ribs, and other small parts. The more similar the size and material of the model to the actual target are, the closer the echo characteristic to the actual target is, and a large-scale scaled model is an effective

method of studying the acoustic reflection characteristics of a target object. Moreover, such a model can achieve strong controllability and provides accurate measurement of target characteristics. This is the primary direction of practice research.

In this study, a high-performance test facility was used to test large-scale underwater complex targets under single base and bistatic conditions. The azimuth and echo intensity of a strong target echo source were predicted using the planar element method. The characteristics of the target echo were studied under the bistatic condition, and the fine feature of target echo energy distribution was studied under the single base condition.

2. Theoretical Analysis and Simulation Analysis

In studies of the large-scale model transmission mechanism of the outer shell and ribbed plate of an actual target, they are approximately regarded as flat plates on two sides of water. Thus, the transmission coefficients of flat plates with

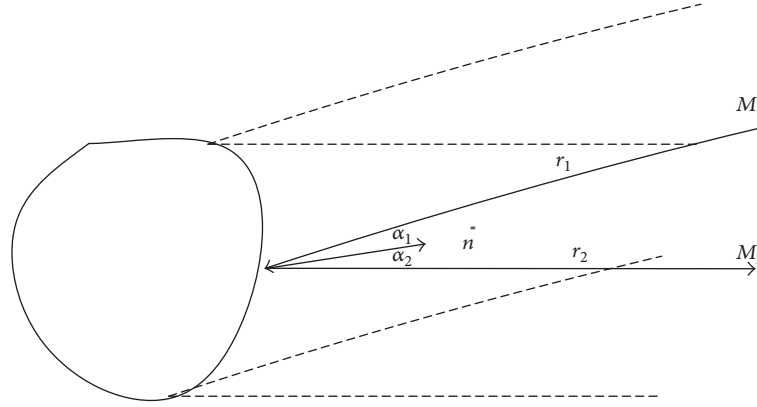


FIGURE 1: Schematic of sound ray.

different thicknesses are calculated and analyzed. Because a nonpressure shell is thin, energy is transmitted throughout a test band. Thus, the objective strength of the nonpressure shell is extremely low and can be neglected in simulations. When the incident angle is 90° , ribbed plate backreflection is extremely weak, and a pressure shell plays a major role in echo.

As shown in Figure 1, the time factor $\exp(-i\omega t)$ is omitted, and the incident wave potential function φ_i is set.

$$\varphi_i = \left(\frac{A}{r_1}\right) \exp(ikr_1) \quad (1)$$

A sound wave is incident from point M_1 to surface S , and the scattered sound field at point M_2 is calculated. The Helmholtz integral equation of the scattering problem is applied as follows:

$$\vartheta_s(\vec{r}_2) = -\frac{1}{4\pi} \int_S \left[\vartheta_s \frac{\partial}{\partial n} \left(\frac{e^{ikr_2}}{r_2} \right) - \frac{\partial \vartheta_s}{\partial n} \frac{e^{ikr_2}}{r_2} \right] dS \quad (2)$$

where \vec{n} is the outer normal of the surface. The Kirchhoff approximation is derived under the condition that the far-field condition is not satisfied, and the scattered sound field is obtained under the bistatic base condition.

$$\vartheta_s(\vec{r}_2) = -\frac{A}{4\pi} \int_{S_0} \frac{e^{ik(k_1+k_2)}}{r_1 r_2} \left(\frac{ir_2 - 1}{r_2} \cos \alpha_1 + \frac{ir_1 - 1}{r_1} \cos \alpha_2 \right) dS \quad (3)$$

According to the definition, the backscatter area is

$$\sigma = \lim_{r_0 \rightarrow \infty} \left(4\pi r_0^2 \left| \frac{\varphi_s}{\varphi_i} \right|^2 \right) = \frac{k^2}{\pi} |I|^2 \quad (4)$$

Therefore

$$TS = 10 \log \left(\frac{\sigma}{4\pi} \right) = 10 \log \left(\frac{1}{\lambda^2} |I|^2 \right) \quad (5)$$

For the single base condition,

$$\vartheta_s = -\frac{A}{2\pi} \int_{S_0} \frac{e^{ikr}}{r^2} \left(\frac{ikr - 1}{r} \cos \alpha \right) dS \quad (6)$$

According to the definition, the backscatter area is

$$\sigma(\vec{r}_1, \vec{r}_2) = \lim_{r_2 \rightarrow \infty} \left(4\pi r_2^2 \left| \frac{\varphi_s(\vec{r}_2)}{\varphi_i(\vec{r}_1)} \right|^2 \right) = \frac{k^2}{\pi} |I|^2 \quad (7)$$

Therefore

$$TS(\vec{r}_1, \vec{r}_2) = 10 \log \left(\frac{\sigma(\vec{r}_1, \vec{r}_2)}{4\pi} \right) = 10 \log \left(\frac{1}{\lambda^2} |I|^2 \right) \quad (8)$$

It is difficult to directly apply the rigorous theory to solve the scattering sound field and the analysis of the echo characteristic of the complex target. In the application of the planar element method [14], it is assumed that the target surface is divided into an $N \times M$ grid. The segmented step length is $1/6$ wavelengths, and I is obtained by the sum of plate element integrals. Using (5) and (8), the bistatic and single base target strength of the entire target is calculated.

2.1. Ribbed Plate and Inner Shell Simulation under Bistatic Base Condition. It is known from Figure 2 that theoretical simulations show that except for a maximum value of $\theta = 90^\circ - \beta/2 = 55^\circ$ (θ is the incident angle, and β is the split angle) there is a high peak close to an incident angle of 145° . Moreover, when the incident angle is 145° , the ribbed plates are perpendicular to the middle line of the incident sound ray and reflected sound ray. This peak is caused by reflection from the ribbed plates.

2.2. Ribbed Plate and Inner Shell Simulation under Single Base Condition. At the experimental distance, the target can be decomposed into three parts: similar cone structure of the bow, similar cone structure of the stern, and main cylindrical structure. Their target strength and azimuth characteristics are shown in Figures 3 and 4.

In the test range, the simulation results show that the maximum echo of the similar cone structure of the bow, the similar cone structure of the stern, and the main cylindrical structure appears at 82.3° , 99.8° , and 90° , respectively.

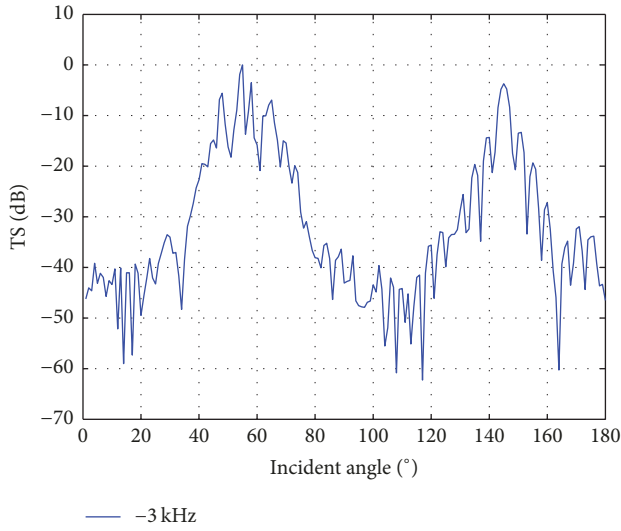


FIGURE 2: Simulation results when the split angle is 70°.

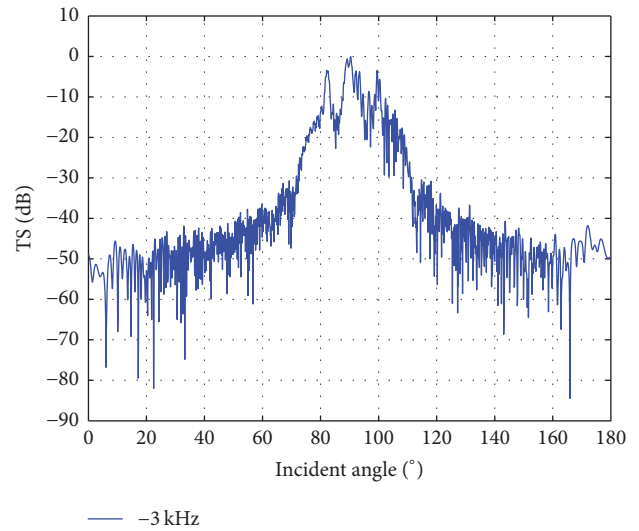


FIGURE 4: Target strength and azimuth characteristics.

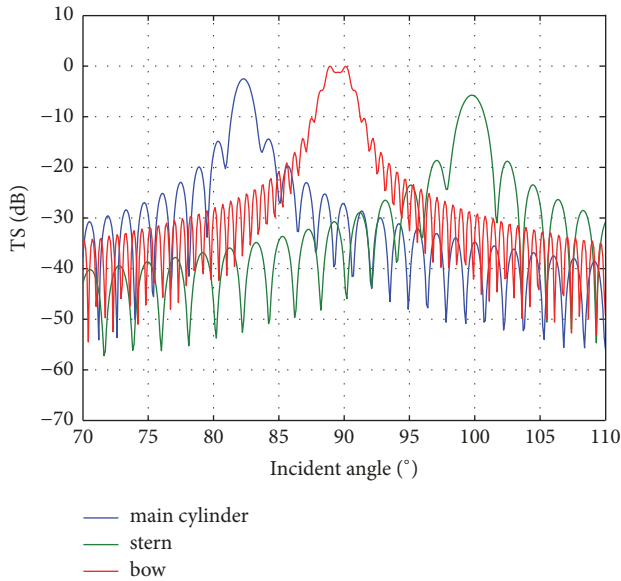


FIGURE 3: Target strength and azimuth characteristics of each part.

3. Experimental Verification

The Dalian Scientific Test and Control Technology Institute conducted an experimental study in the southern Dalian sea at a low frequency to study the broadband and multistation echo characteristics of a large-scale underwater complex target scaled model.

3.1. Experimental Implementation under Bistatic Base Condition. As shown in Figures 5 and 6, an emission array is mounted at the stern of a measuring ship, and the model is mounted on the first hanger rod of the ship’s water well. The model enters the water at 10 m, comprising a 5 m hanger rod and a 5 m soft connection portion. The auxiliary ship is outfitted with a separate receiving system. The split

angle (β) is fixed, and the submarine model rotates to obtain omnidirectional echo data of the model.

3.2. Experimental Implementation Process under Single Base Condition. As shown in Figures 5 and 6, a transmitting and receiving transducer array is fixed on the same hanger rod, and the depth of the sound center is consistent with the depth of the submarine model waterline. A continuously rotating submarine model is considered, in which the rotation angle ranges within 0–180°, and the broadband echo of the submarine model is tested.

4. Data Analysis

4.1. Echo Intensity Azimuth Characteristics under Bistatic Base Condition. As shown in Figures 7 and 8, the target echo intensity is at the maximum when the incident angle is 56.2°. At this time, the midline direction of the transmitted and received “split angle” is the vertical target axis direction. Therefore, the echo intensity is the highest; its value is close to the maximum target strength value of 90° under the single base condition. In addition to the maximum at the incident angle of 56.2°, there is a peak at an incident angle of 146.5°, and the echo intensity is approximately 10 dB lower than the echo intensity at 56.2°.

4.2. Strong Reflection Source Analysis under Bistatic Base Condition. When the split angle is 68°, the azimuth of the incident angle of 56.2° is the abeam azimuth. Figure 9 and Table 1 show the distribution of the abeam azimuth strong reflection source.

When the incident angle is in the abeam direction under the bistatic base condition, the energy of the echo primarily results from the reflection of the outer shell, inner shell, fairwater, and flexural wave. The total energy of the inner shell in the strong reflection azimuth is more than 55% of the total energy of the echo. As shown in Figures 8 and 9, the reflection

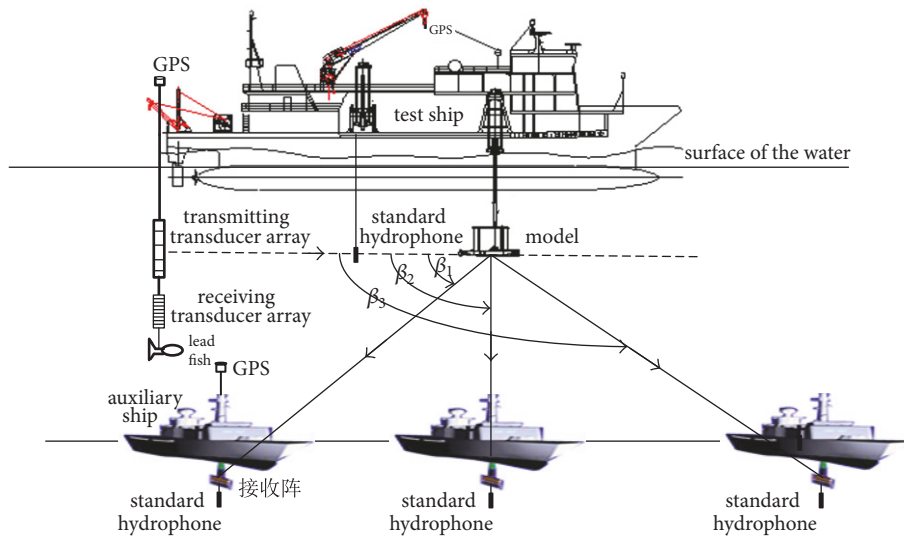


FIGURE 5: Experimental implementation plan.

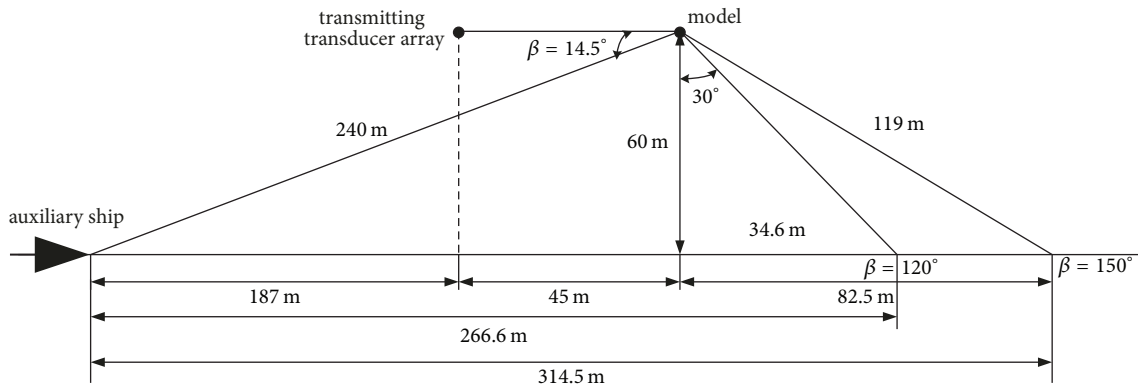


FIGURE 6: Auxiliary ship maneuver mode.

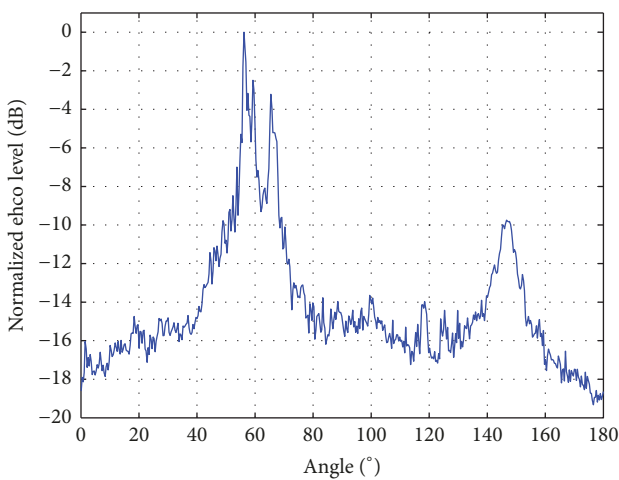


FIGURE 7: Echo intensity 2D azimuth characteristics.

Close to an incident angle of 56° , there are three echo pulses after the hull reflection wave. The pulse time intervals are 1.665 ms, 1.619 ms, and 1.665 ms according to the target, the transmitting and receiving array, and seabed and surface geometry, respectively. The minimum sea surface multipath echo is 2.17 ms, and the minimum seabed multipath echo is 16.68 ms. It can be concluded that the three echo pulses are not multipath echoes but elastic echoes.

At this time, the target can be approximated as a finite cylindrical shell, with $Ka = 35$, where K is the wave number and a is the thickness of the cylindrical shell. Because of the larger Ka , the target can be approximated using flat plate results. The coincidence frequencies of the steel plate and target are $fh = 0.2 \text{ MHz}\cdot\text{mm}$ and $fh = 0.15 \text{ MHz}\cdot\text{mm}$, respectively. Coincidence resonance occurs as these frequencies are similar. According to the cylindrical shell theory [14] by Marston et al., the frequency of the flexural wave does not reach the coincidence frequency and the flexural wave is subsonic. The sound velocity of the flexural wave is 1132 m/s, and the primary part of the flexural wave is a subsonic A0 wave [14]. The total energy of the flexural wave is 13.5% of the total energy of the echo.

of the inner shell plays a major role at approximately 15° from the abeam azimuth.

TABLE 1: Distribution values of the abeam azimuth strong reflection source.

60° strong reflection source	Abeam outer shell	Inner shell	Fairwater 1	Fairwater 2	Flexural wave 1	Flexural wave 2	Flexural wave 3	Total
Energy ratio	3.4	56.5	14.0	9.2	10.9	1.9	0.7	97.6

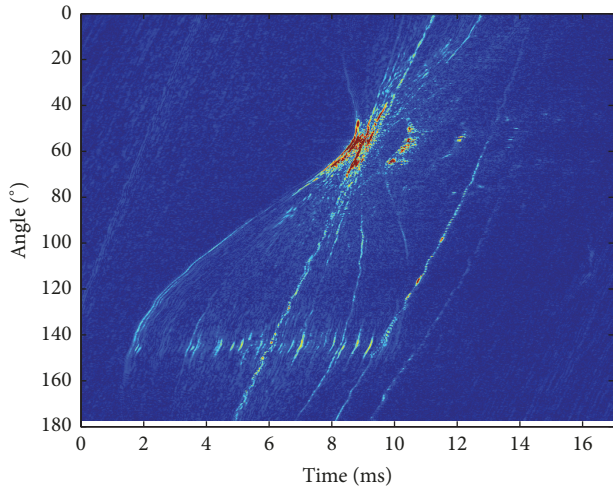


FIGURE 8: Echo intensity 3D azimuth characteristics.

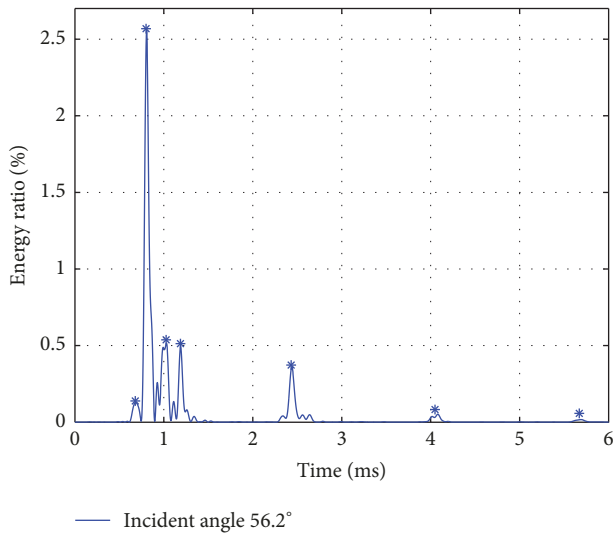


FIGURE 9: Energy distribution in abeam azimuth.

As shown in Figure 10 and Table 2, the incident angle is 146.5°, the axis of the target is parallel to the midline direction of transmitting and receiving sound ray, and the energy of the echo is primarily from the ribbed plate. The total energy of the ribbed plate is approximately 80% of the total energy of the echo.

4.3. Echo Intensity Azimuth Characteristics under Single Base Condition. As shown in Figures 11 and 12, the echo maximum of similar cone structure of the bow, similar cone structure of the stern, and the main cylindrical structure appears at

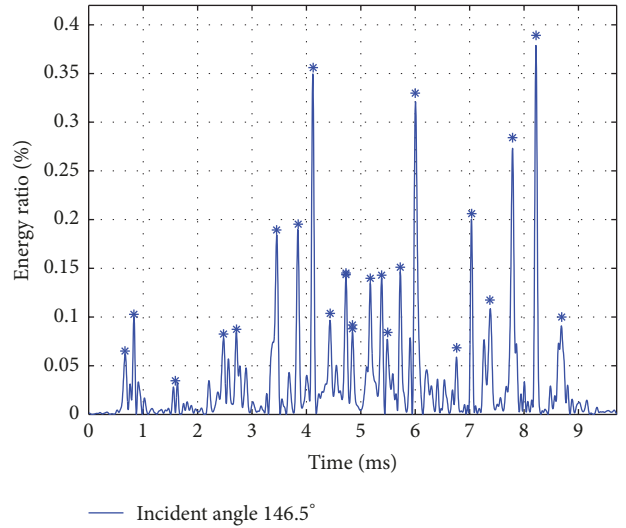


FIGURE 10: Energy distribution at submaximum point of echo intensity.

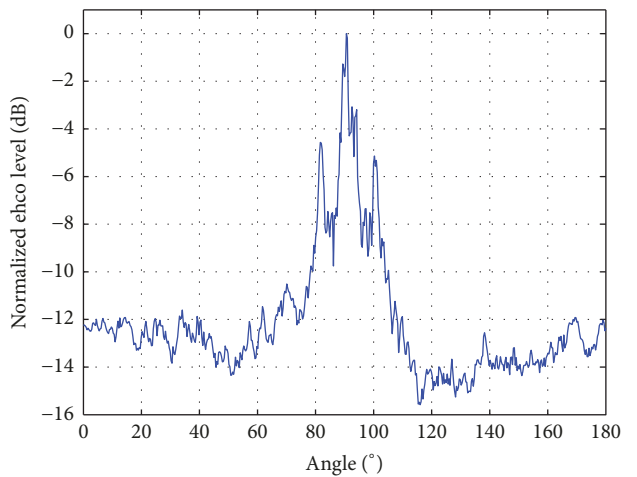


FIGURE 11: Echo intensity 2D azimuth characteristics.

81.6°, 100.3°, and 90°, respectively. The comparison between theoretical simulation and experimental results is shown in Table 3.

4.4. Strong Reflection Source Analysis under Single Base Condition. As shown in Figures 13 and 14 and Table 4, sound waves are incident from the model header, and echo energy primarily results from the ribbed plate and fairwater. The total energy of the ribbed plate is approximately 60% of the total energy of the echo, and the total energy of the fairwater is

TABLE 2: Ribbed plates and their energy ratios.

Ribbed plate	1	2	3	4	5	6	7	8	Total Energy ratio
Energy ratio	1.5	1.8	0.9	3.2	3.7	5.9	3.8	6.4	
Ribbed plate	9	10	11	12	13	14	15	16	
Energy ratio	2.8	3.0	1.8	4.2	3.0	1.7	3.0	1.2	
Ribbed plate	17	18	19	20	21	22	23	24	
Energy ratio	8.1	1.0	3.3	1.7	2.8	8.0	7.0	1.9	81.9

TABLE 3: Comparison of theoretical and experimental results.

Result	Similar cone of the bow (°)	Main cylindrical structure (°)	Similar cone of the stern (°)	Remarks
Test result	81.6	90.6	100.3	Test distance
Theoretical research	81.9	90	99.5	Test distance and target size
Simulation study	82.3	90	99.8	Test distance and target size
Theoretical research	85	90	96.4	Far field and target size
Simulation study	85	90	96	Far field and target size

TABLE 4: Ribbed plate energy ratio of the bow.

Ribbed plate	1	2	3	4	5	6	7	8	9	Total Energy ratio
Energy ratio	1.9	3.3	5.1	1.4	1.9	2.9	1.6	4.3	1.6	
Ribbed plate	10	11	12	13	14	15	16	17	18	
Energy ratio	3.2	2.0	1.5	2.9	3.0	2.7	6.4	7.0	1.7	
Ribbed plate	19	20	21	22	23	24	25	26		
Energy ratio	1.6	3.3	1.1	2.43	1.7	1.7	0.6	0.5		74.5

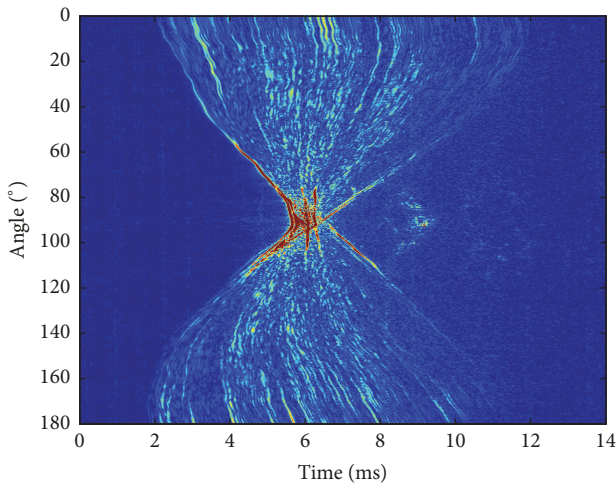


FIGURE 12: Echo intensity 3D azimuth characteristics.

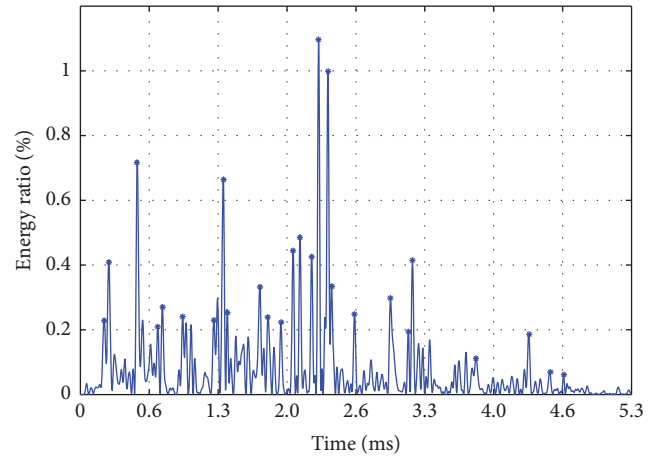


FIGURE 13: Echo intensity 2D azimuth characteristics of the bow.

approximately 15% of the total energy of the echo. Because of the ribbed plate block, rib echo is not clear and elastic echo is not evident.

As shown in Figures 15, 16, and 17 and Table 5, in the abeam azimuth ($\pm 15^\circ$), the energy of the echo primarily results from the reflection of the outer shell, inner shell, and fairwater. In the strong reflection azimuth, the reflection energy of the inner shell exceeds 60% of the total energy of the echo, and the total energy of the strong echo source

exceeds 90% of the total energy of the echo. In the nonstrong reflecting azimuth, the reflection energy of the inner shell accounts for approximately 10%–20% of the total energy of the echo, and it is equivalent to several other strong reflection sources. The total energy of the strong echo source is more than 85% of the total energy of the echo.

There is a clear flexural wave after the hull reflection wave, and the sound velocity is 1109 m/s, which is the subsonic A0 wave. The maximum energy of the flexural wave is 7.6% of the echo energy, and the maximum angle is 88° .

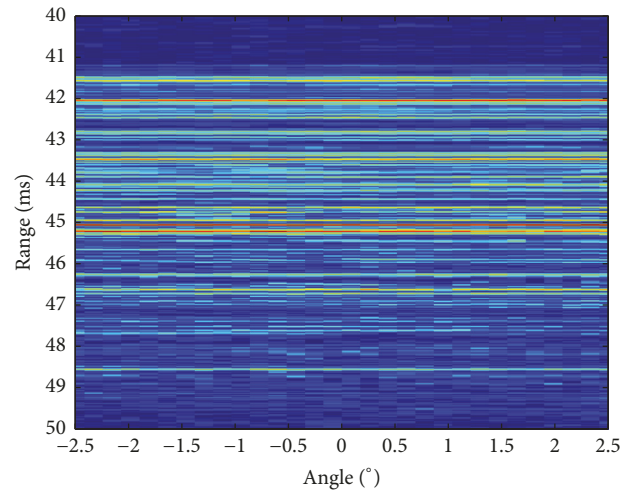


FIGURE 14: Echo intensity 3D azimuth characteristics of the bow.

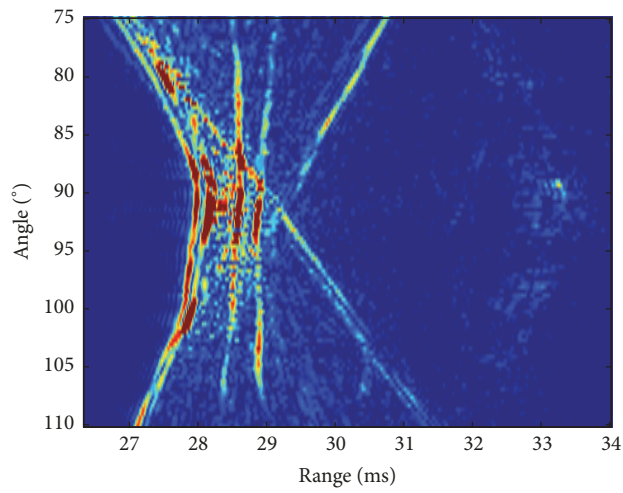


FIGURE 15: Echo intensity 3D azimuth characteristics in abeam azimuth.

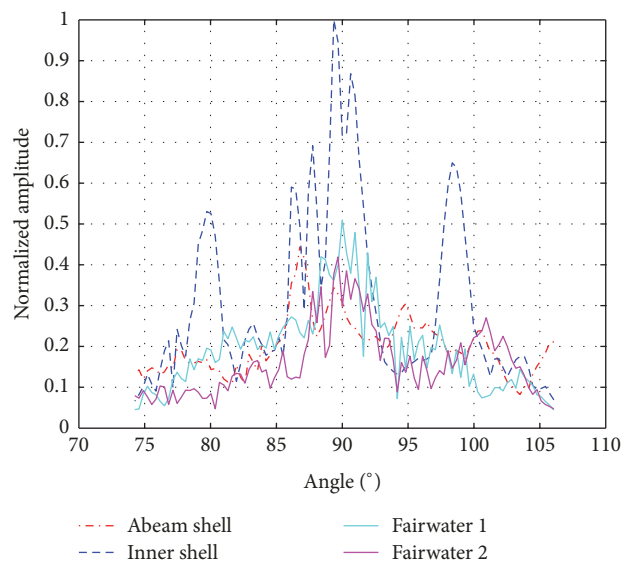
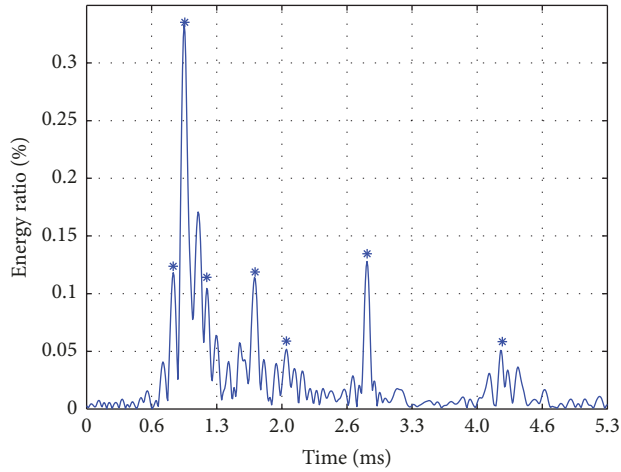
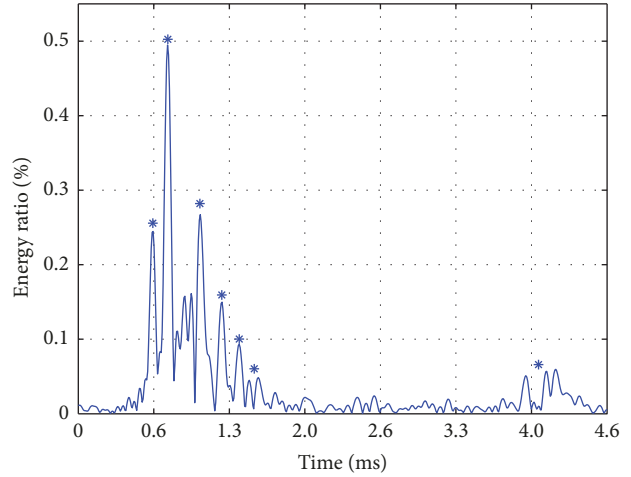


FIGURE 16: Echo intensity 2D azimuth characteristics in abeam azimuth.



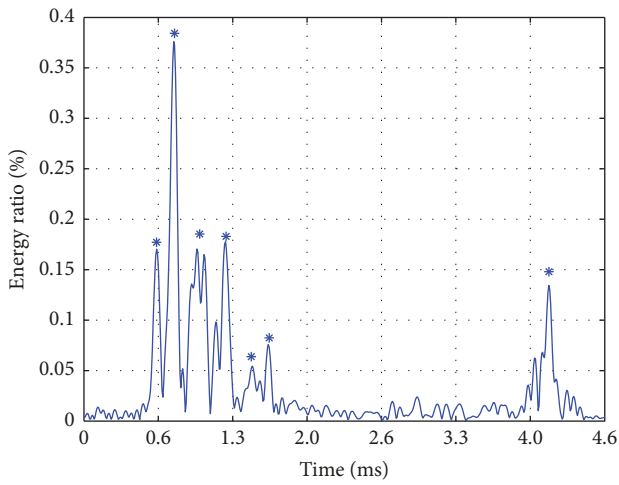
— Incident angle 81.6°

(a) Incident angle is 81.6°



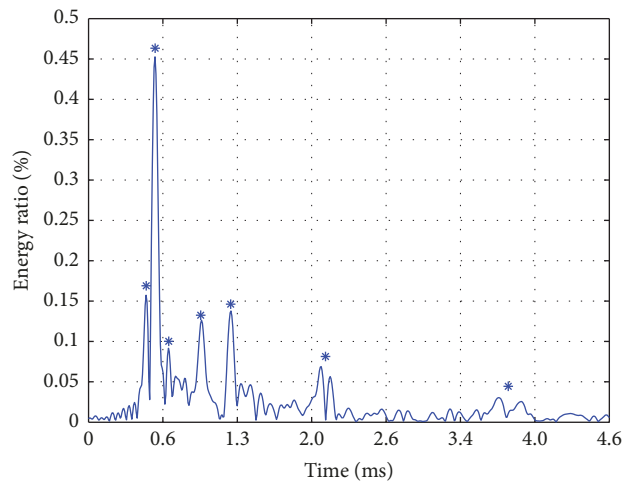
— Incident angle 90.6°

(b) Incident angle is 90°



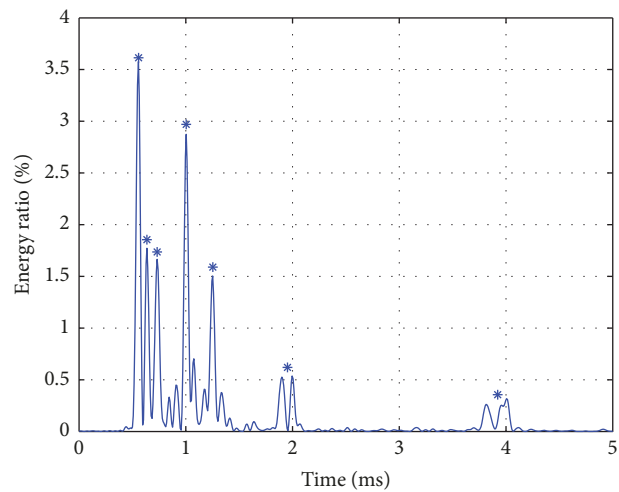
— Incident angle 92°

(c) Incident angle is 92°



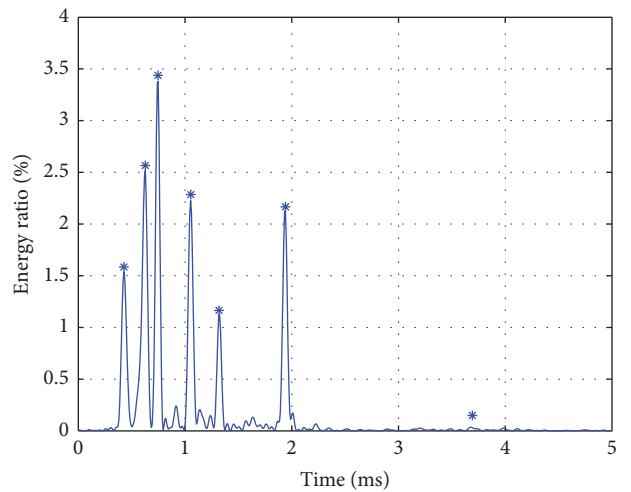
— Incident angle 100.3°

(d) Incident angle is 100.3°



— Incident angle 84°

(e) Incident angle is 84°



— Incident angle 97°

(f) Incident angle is 97°

FIGURE 17: Typical azimuth echo intensity 2D energy ratio.

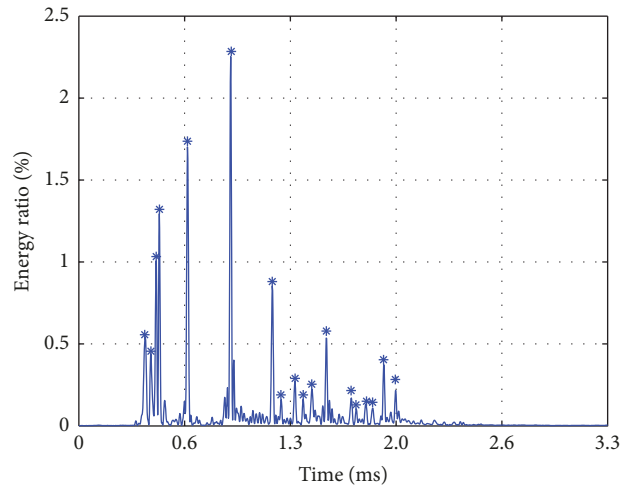


FIGURE 18: Echo intensity 2D azimuth characteristics of the stern.

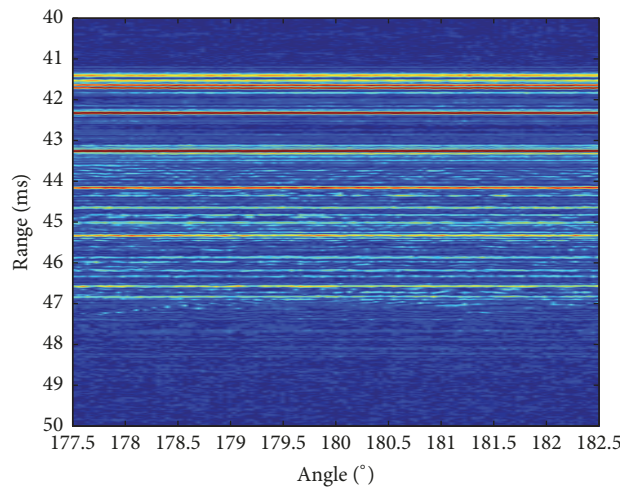


FIGURE 19: Echo intensity 3D azimuth characteristics of the stern.

When the acoustic wave is obliquely incident (15° – 75° , 105° – 165°), the primary reflected energy of the outer shell, inner shell, and fairwater cannot be returned to the direction of incidence. The geometrical scattering of the ribbed plate, outer rib, and fairwater plays a major role, accounting for approximately 70% of the total energy of echo. The geometric reflection of the outer shell and inner shell is not strong, and the elastic echo is not evident.

As shown in Figures 18 and 19 and Tables 6 and 7, sound waves are incident from the tail of the model and echo energy primarily results from the ribbed plate. The total echo energy of the ribbed plate is approximately 75% of the total echo energy. The echoes of the inner and outer ribs are clear. The echo energies of each outer rib and each inner rib are approximately 0.5% and 0.1% of the total echo energy, respectively. The inner rib echo is elastic waves caused by discontinuities in the welded joint, and the elastic echo of other parts is not evident.

4.5. *Frequency Domain Characteristics.* The frequency domain analysis of the target echo shows that the energy of

the echo signal varies with time. Thus, the energy distribution characteristic of the wideband echo in each frequency band is obtained, which reflects the target reflection and scattering ability.

As shown in Figures 12 and 21(b), eight large bright lines appear between 0° – 75° and 115° – 180° , and the number of interference fringes increases linearly with frequency. This is Bragg scattering by periodic ring ribs and nonperiodic rib generation. The flexural wave caused by the ribs and the elastic echo caused by the resonance of the ribs are not evident.

Comparing Figures 20 and 21(a), the spectrum of a single bright spot is smooth, and the spectrum of the synthesized highlights shows eight distinct small lines, indicating that interference exists between the strong reflection sources at 75° – 115° .

5. Conclusions

(1) For the corresponding entity object, in the 2–4 kHz band, clear flexural waves are observed in the abeam azimuth. There

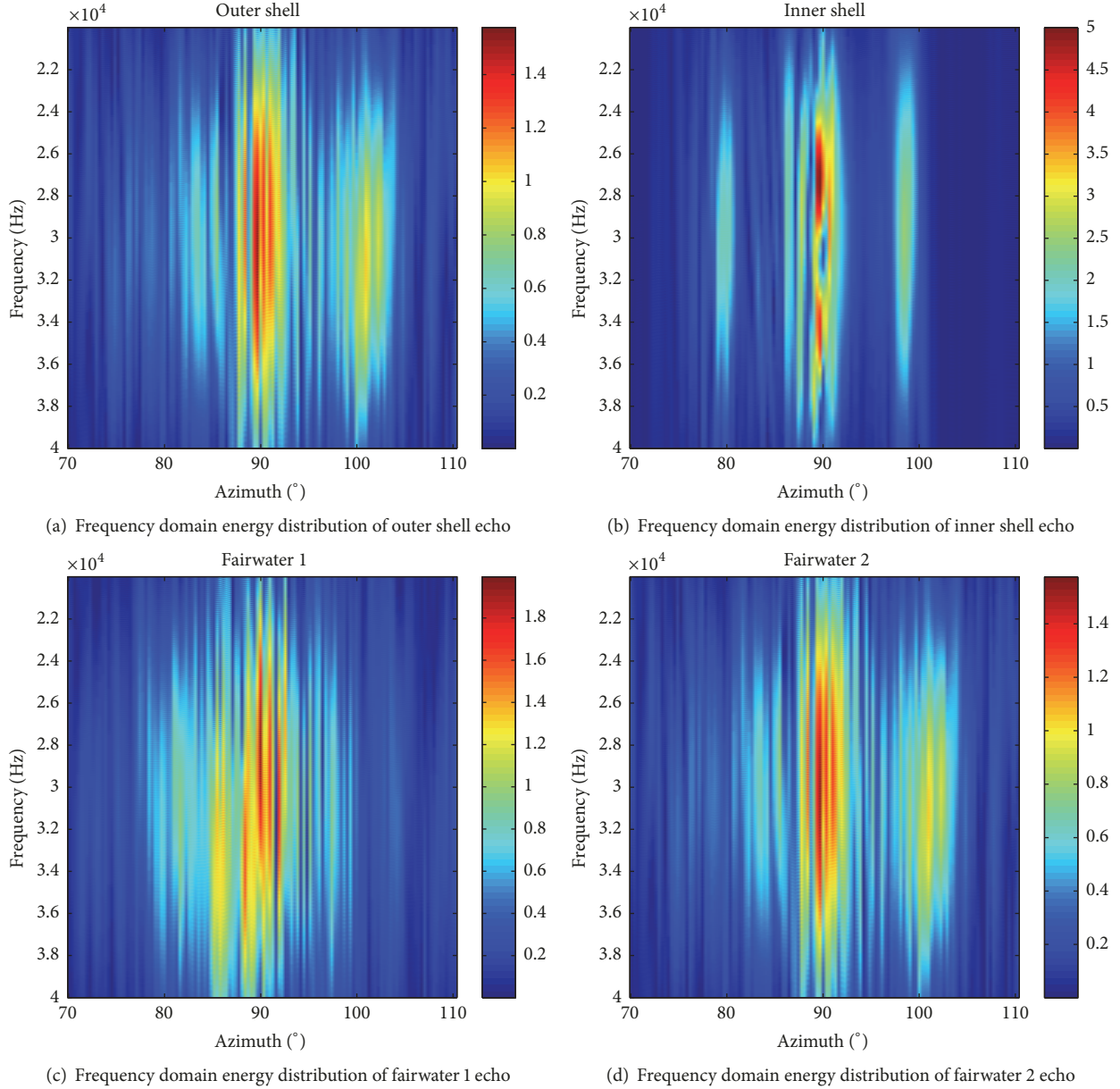


FIGURE 20: Frequency domain energy distribution of strong reflection source in abeam azimuth.

are three echo pulses under the bistatic base condition. The sound velocity of the flexural wave is 1132 m/s, and the total energy of the flexural wave is 13.5% of the total energy of the echo; the maximum angle is 56.2° . There is a clear flexural wave under the single base condition, and the sound velocity is 1109 m/s. The maximum energy of the flexural wave is 7.6% of the echo energy, and the maximum angle is 88° .

(2) Under the bistatic base condition, except for a maximum value of $\theta = 90^\circ - \beta/2 = 55^\circ$, there is a high peak close to an incident angle of 145° , and the echo intensity is approximately 10 dB lower than the echo intensity at 56.2° . When the incident angle is 145° , this peak is caused by reflection from the vertical ribbed plates at the middle line of the incident sound ray and reflected sound ray. The echo

energy of the ribbed plate is approximately 80% of the total echo energy.

(3) Under the single base condition, the energy of the echo primarily results from the reflection of the outer shell, inner shell, and fairwater in the abeam azimuth. In the strong reflection azimuth, the reflection energy of the inner shell exceeds 60% of the total energy of the echo, and the total energy of the strong echo source exceeds 90% of the total energy of the echo. In the nonstrong reflecting azimuth, the reflection energy of the inner shell accounts for $\sim 10\text{--}20\%$ of the total energy of the echo, and it is equivalent to several other strong reflection sources. The total energy of the strong echo source is more than 85% of the total energy of the echo. When sound waves are incident from the head and tail of the

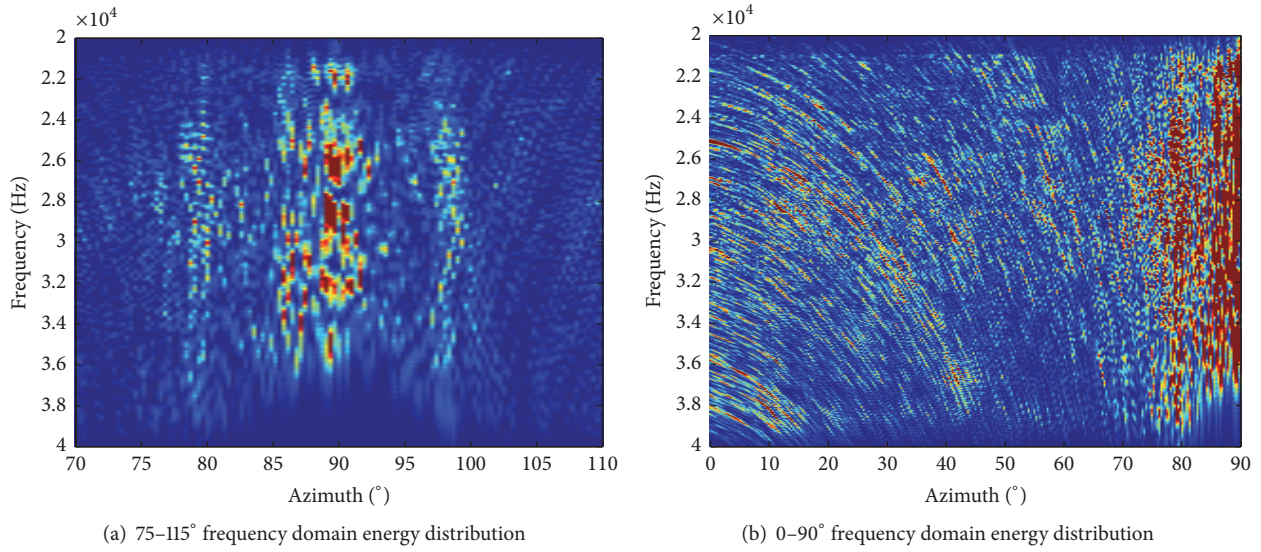


FIGURE 21: Frequency domain energy distribution under single base condition.

TABLE 5: Energy ratio of strong reflection source.

100.3° strong reflection source	Abeam shell	Inner shell similar cone of the stern	Fairwater 1	Fairwater 2	Stern outer shell	Bow outer shell	Flexural wave	Total
Energy ratio	7.0	72.9	7.1	5.3	0.6	2.4	0.4	95.6
90.6° strong reflection source	Abeam shell	Inner shell main cylindrical structure	Fairwater 1	Fairwater 2	Bow outer shell	Stern outer shell	Flexural wave	Total
Energy ratio	6.8	68.5	10.3	11.0	0.2	0.5	1.0	98.3
81.6° strong reflection source	Abeam shell	Inner shell similar cone of the bow	Bow outer shell	Fairwater 1	Fairwater 2	Stern outer shell	Flexural wave	Total
Energy ratio	4.6	66.8	4.8	7.7	1.7	8.4	2.9	96.8
92° strong reflection source	Abeam shell	Moving bright spot of inner shell	Fairwater 1	Fairwater 2	Stern outer shell	Bow outer shell	Flexural wave	Total
Energy ratio	8.6	60.2	8.2	10.0	1.3	1.5	7.6	97.4
84° strong reflection source	Abeam shell	Moving bright spot of inner shell	Bow outer shell	Fairwater 1	Fairwater 2	Stern outer shell	Flexural wave	Total
Energy ratio	21.4	9.5	11.3	18.2	10.4	7.8	7.0	85.7
97° strong reflection source	Abeam shell	Moving bright spot of inner shell	Fairwater 1	Fairwater 2	Stern outer shell	Bow outer shell	Flexural wave	Total
Energy ratio	11.4	21.0	20.9	15.2	7.1	15.0	0.7	91.2

TABLE 6: Ribbed plate energy ratio at 180°.

Ribbed plate	1	2	3	4	5	6	7	8	9	Total energy ratio
Energy ratio	5.9	3.6	6.2	7.4	12.5	14.4	6.1	1.1	2.0	
ribbed plate	10	11	12	13	14	15	16	17	18	
Energy ratio	1.1	2.0	3.6	1.4	0.7	1.1	0.9	2.7	1.5	74.5

TABLE 7: Outer rib energy ratio at 180°.

Outer rib	1	2	3	5	6	7	8	9	10	Average energy ratio
Energy ratio	1.02	0.72	0.52	0.30	0.54	0.49	0.50	0.44	0.50	0.54

model, the scattering of the ribbed plate and fairwater plays a major role, accounting for approximately 75% of the total energy of echo.

(4) Eight large bright lines appear between 0–75° and 115–180°, and the number of interference fringes increases linearly with frequency, which are characteristic of Bragg scattering by periodic ring ribs and nonperiodic rib generation. The flexural wave caused by ribs and the elastic echo caused by the resonance of ribs are not evident. The spectrum of a single bright spot is smooth, and the spectrum of the synthesized highlights shows eight distinct small bright lines, indicating that interference exists between the strong reflection sources at 75–115°.

Conflicts of Interest

There are not any ethical/legal conflicts involved in the article.

Authors' Contributions

All authors have read and approved the content and agreed on submission for consideration for publication in the journal.

Acknowledgments

This work was supported by the Pre-Research Project of the Science and Technology on Underwater Test and Control Laboratory (no. 41416020301).

References

- [1] G. C. Gaunaurd and M. F. Werby, "Sound scattering by resonantly excited, fluid-loaded, elastic spherical shells," *The Journal of the Acoustical Society of America*, vol. 90, no. 5, pp. 2536–2550, 1991.
- [2] X. Shen, H. Li, K. Li, X. Cao, and Q. Yang, "Some differential geometric relations in the elastic shell," *Mathematical Problems in Engineering*, vol. 2016, Article ID 1463823, 9 pages, 2016.
- [3] G.-Y. Zheng, J. Fan, and W.-L. Tang, "Low-frequency echo from finite ring-stiffened double cylindrical shells: approximate theory and experiment," *Journal of Ship Mechanics*, vol. 15, no. 12, pp. 1451–1462, 2011.
- [4] M. L. Rumerman, "Increased accuracy in the application of the Sommerfeld-Watson transformation to acoustic scattering from cylindrical shells," *The Journal of the Acoustical Society of America*, vol. 90, no. 5, pp. 2739–2750, 1991.
- [5] W. Fan, G. Zheng, and J. Fan, "Analysis of circumferential waves on a water-filled cylindrical shell," *Acta Acustica*, vol. 35, no. 4, pp. 419–426, 2010.
- [6] M. Tran-Van-Nhieu, "Scattering from a ribbed finite cylindrical shell," *The Journal of the Acoustical Society of America*, vol. 110, no. 6, pp. 2858–2866, 2001.
- [7] G.-Y. Zheng, J. Fan, and W.-L. Tang, "Acoustic scattering from water-filled finite cylindrical shell in water," *ACTA ACUSTICA*, vol. 35, no. 1, 2010.
- [8] M. Tran-Van-Nhieu, "Scattering from a ribbed finite cylindrical shell with internal axisymmetric oscillators," *The Journal of the Acoustical Society of America*, vol. 112, no. 2, pp. 402–410, 2002.
- [9] F. Jun, *Study on echo characteristics of underwater complex targets*, Doctoral Dissertation of Shanghai Jiao Tong University, 2002.
- [10] P. An, F. Jun, and Z. Lin-Kai, "Acoustic scattering from a finite periodically bulkheads in cylindrical shell," *Acta Physica Sinica*, vol. 61, no. 21, Article ID 214301, 2012.
- [11] P. An, F. Jun, and Z. Lin-Kai, "Acoustic scattering from a finite quasi-periodic bulkhead cylindrical shell," *Acta Physica Sinica*, vol. 62, no. 2, Article ID 024301, 2013.
- [12] C. Yun-Fei, L. Gui-Juan, W. Zhen-Shan, Z. Ming-Wei, and J. Bing, "Statistical feature of underwater target echo highlight," *Acta Physica Sinica*, vol. 62, no. 8, Article ID 084302, 2013.
- [13] B. Zhang, T.-S. An, J. Han, Z.-C. Ma, and L.-G. Zhu, "Extracting fine details in broadband echoes from complex underwater targets," *Journal of Harbin Engineering University*, vol. 31, no. 7, pp. 872–878, 2010.
- [14] P. L. Marston and N. H. Suna, "Backscattering near the coincidence frequency of a thin cylindrical shell: Surface wave properties from elasticity theory and an approximate ray synthesis," *The Journal of the Acoustical Society of America*, vol. 97, no. 2, pp. 777–783, 1995.

